Available online at www.sciencedirect.com
ScienceDirect
International Journal of Heat and Fluid Flow 29 (2008) 292–305
International Journal of HEAT AND FLUID FLOW
www.elsevier.com/locate/ijhff

CFD study of the hydraulic and thermal behavior of spherical-void-phase porous materials

S.A. Mohsen Karimian, Anthony G. Straatman *

The University of Western Ontario, Department of Mechanical and Materials Engineering, London, Ontario, Canada N6A 5B9

Received 8 January 2007; received in revised form 14 June 2007; accepted 5 July 2007
Available online 24 August 2007

Abstract

To investigate the feasibility of the use of foams with an interconnected spherical pore structure in heat transfer applications, models for heat transfer and pressure drop for this type of porous materials are developed. Numerical simulations are carried out for laminar periodic, thermo-fluid flow in an idealized pore geometry of foams with a wide range of geometry parameters. Semi-heuristic models for pressure drop and heat transfer are developed from the results of simulations. The model developed for pressure drop is based on Carman–Kozeny theory. An Ergun-like quadratic extension is added to the model for higher Reynolds number regimes. The variation of the resulting Kozeny constant is consistent with that reported in literature for other types of pore geometry. Presence of a cubic behavior of pressure drop in terms of velocity in the weak inertia flow regime was explored and observed, which was in agreement with the theory of weak inertia flow in existing literature. A heat transfer model is developed using parametric study on the data from the simulations. The proposed models can be used as outlines for future experimental studies.

Keywords: Heat transfer model; Hydraulic model; Porous media; Metallic foam; Graphitic foam; Non-Darcy flow; Weak inertia regime; Convective heat transfer

1. Introduction

Many porous materials have an open, interconnected void structure that makes the internal surface area of the media accessible to fluid. Such materials include high-porosity reticulated metal foams that are formed by casting, and more moderate-porosity graphitic foams that are formed by a process of foaming and heat treatment of a carbon precursor (Klett et al., 2000; Gallego and Klett, 2003). Compared to reticulated metal foams, graphitic foams have a higher internal surface area to volume ratio and a higher solid-phase conductivity, which make them a suitable candidate for convective heat transfer applications. The high solid-phase conductivity of graphitic foam leads to a high effective (stagnant) conductivity ($k_e = 40$–160 W/m K) which enables the heat to penetrate deeply into the solid structure of the foam thereby increasing the possibility of thermal non-equilibrium condition in the fluid–solid interaction and the convective heat transfer. With increasing interest in using graphitic foams in convective heat transfer applications, see for example Tadrist et al. (2004) and Yu et al. (2006a), it is of interest to develop flow and heat transfer models for this type of foam structure to further investigate the feasibility of implementation.

Starting with Darcy's experiment (Darcy, 1856) and his introduction of permeability, the flow and heat transfer inside porous media has been extensively studied. A thorough review of studies in this area can be found in Dullien (1979) and Kaviany (1999). In most of the studies, however, it is assumed that a packed bed of spherical particles is the common microscopic structure of porous media. The microscopic structure of foams is completely different than

* Corresponding author. Tel.: +1 519 661 2111x88249; fax: +1 519 661 3020.
E-mail addresses: skarimi2@uwo.ca (S.A. Mohsen Karimian), astraatman@eng.uwo.ca (A.G. Straatman).

0142-727X/$ - see front matter © 2007 Elsevier Inc. All rights reserved.
doi:10.1016/j.ijheatfluidflow.2007.07.003

that of a packed bed of spherical particles and varies significantly with the porosity and pore size. At the higher end of porosity and pore size, reticulated foams such as aluminum foams with a porosity of $\epsilon > 0.9$ and a pore size of $D_p \sim O(\text{mm})$ are modeled accurately as a network of interconnected fibers or ligaments; see for example Fourie and Du Plessis (2002). Based on such geometry models, studies on the hydraulic and thermal characteristics of reticulated foams have been carried out by, for example, Calmidi and Mahajan (1999, 2000) and Boomsma et al. (2003). On the other side of the spectrum, the microscopic structure of graphitic foam with a more moderate porosity of $\epsilon = 0.7$–0.9 and pore size of $D_p \sim O(\mu\text{m})$ is characterized as a network of interconnected spherical pore structures. A geometry model for the internal structure of graphitic foam has been proposed by Yu et al. (2006b). The model is based on interconnected sphere-centered cubes, where the interconnected spheres represent the void phase of the porous media. Combining elements of this idealized geometry with experiments, Straatman et al. (2006) conducted a study of the heat transfer and hydraulic losses associated with graphitic foam. No detailed information at the pore-level was presented.

To properly develop hydraulic and thermal models for foams with moderate porosity such as Graphitic Foam and Carbon Foam, a study of the pore-level thermo-fluid flow inside the interconnected pores of spherical-void-phase (SVP) foams is necessary. Experimental studies of the flow structure at that level would suffer from lack of instrumentation, leading to poor measurement resolution. Thus, semi-heuristic hydraulic and thermal models based on the results of direct numerical simulations of the flow and energy fields inside an idealized representation of the SVP foam micro-structure is a proper start. A solution of this type will indicate the general characteristics of the real flow, but will not necessarily replicate accurately the physics of the real flow field since in this ideal case, the foam structure is assumed to be perfectly periodic and homogeneous. The main purpose of these models is to recognize the importance of each parameter on the governing behavior of the fluid flow and heat transfer at the pore level. Such models can be used to guide experimental investigations at the macroscopic scale.

The hydraulic behavior in the idealized cell structure is characterized herein using conventional relations developed for porous media. These relations are categorized as permeability models, which model creeping flow behavior using Darcy's law, and extended models, which model strong inertia flow by adding non-linear extensions to permeability models. Among permeability models, the hydraulic radius model known as Carman–Kozeny model (Dullien, 1979) provides the best general relation for estimating pressure drop across a porous media with moderate porosity. Since this model was primarily developed for packed beds of spherical particles, it is necessary to re-visit and modify the model for foams with a spherical interconnected pore structure. For flow with high Reynolds number, Forchheimer (1901) suggested that a quadratic extension to the Darcy's law can approximately model the pressure behavior. Ergun (1952) proposed a quadratic extension to the Carman–Kozeny model, based on the analogy of the inertial forces compared to the viscous forces. This extension must also be re-visited for the geometry of interest herein.

The cubic behavior of pressure drop in the weak inertia flow regime in terms of velocity was experimentally recognized by Muskat (1946) and was mathematically shown by Mei and Auriault (1991). Firdaouss et al. (1997) proved that some legendary experiments including that of Darcy and Forchheimer qualitatively follow the cubic model proposed by Mei et al. for weak inertia flows. The cubic behavior of pressure drop in the weak inertia flow regime has also been observed and verified by others, see for example Rojas and Koplik (1998), Kim et al. (2001), Spena and Vacca (2001) and Fourar et al. (2004) among others. However, a quadratic extension to a permeability model is still a good engineering approximation for both weak and strong inertia flow. Therefore, while verifying the presence of a cubic pressure drop in the weak inertia flow regime is considered in this work, the proposed model will be bound to an Ergun-like quadratic extension.

By using the concept of periodicity, Karimian and Straatman (2007) adopted the logarithmic law (Incropera and DeWitt, 2002) to calculate the pore-level Nusselt number for a periodic cell. A convective heat transfer model is proposed herein based on computed pore-level Nusselt numbers of a similar form.

In the present work, suitable general forms of engineering models for characterizing the hydraulic and thermal behavior of flow in foams with a spherical interconnected pore structure are proposed based on the results of direct numerical simulation of unidirectional thermo-fluid flow through an idealized unit-cube cell. The proposed general forms can be calibrated using experimental investigations. Though the results of the DNS calculations include full details of the pore-level flow structure, the aim of this work is on the development of hydraulic and thermal models and thus the main focus is on the overall pore-level pressure drop and heat transfer provided by the DNS calculations. The representative geometry and the computational domain are defined in the next section. In Section 3, the governing equations, the boundary conditions and the numerical method are given. The numerical simulation setup and the grid convergence study are described in Section 4. The last section describes the development of the hydraulic and thermal models.

2. Computational domain

In this study, we are interested in the flow and heat transfer inside a generic section of a block of foam. Since a foam would typically be comprised of hundreds of cells in each direction, it is suitable to assume that the flow in a generic section inside the foam is periodic in nature and

as such, only a representative portion of domain requires modeling.

Fig. 1 shows electron micrographs of a typical graphitic foam specimen developed at Oak Ridge National Laboratory (ORNL) (Klett et al., 2000). To characterize the internal structure of graphitic foam, Yu et al. (2006b) proposed a unit-cube geometry model. The model is based on interconnected sphere-centered cubes, called unit-cube cells or simply cells, where the interconnected spheres represent the void phase of the porous media. Fig. 2a shows a three-dimensional CAD image of a unit-cube cell. It is assumed that this idealized geometry is the building block of the porous media (as shown in Fig. 2b). In this geometry model, the porous media is assumed homogenous with a periodic internal geometry. A unit-cube cell in Yu et al. (2006b) is defined by the porosity, ϵ (defined as % void phase), of the represented graphitic foam and the pore diameter D_p. Fig. 3 shows the detailed dimensions of the unit-cube model. Here, D_p is the pore diameter, H is the cell size and D_w is the interconnected pore-window diameter. The cell size H is determined as a function of porosity ϵ and pore diameter D_p. The equation relating these three factors can be obtained from the definition of porosity (Yu et al., 2006b):

$$\left(\frac{H}{D_p}\right)^3 - \frac{3\pi}{(4\epsilon+\pi)}\left(\frac{H}{D_p}\right) + \frac{4\pi}{3(4\epsilon+\pi)} = 0. \quad (1)$$

Eq. (1) indicates that

$$\eta = \frac{H}{D_p} = f(\epsilon), \quad (2)$$

where η is the cell ratio. Using the definition of η and the unit-cube model formulations (Yu et al., 2006b), the pore-window diameter D_w can be calculated using:

$$D_w = \sqrt{1-\eta^2} \times D_p. \quad (3)$$

Eqs. (2) and (3) show that for a given porosity, the cell size and the pore-window diameter vary proportional to the pore diameter. Therefore, the pore-level thermo-fluid flow structure can be scaled using pore diameter or one of its products, e.g. cell size or pore-window diameter, as a pore-level length-scale and hence all dimensionless quantities are solely functions of porosity. Details of validation can be found in Karimian (2006).

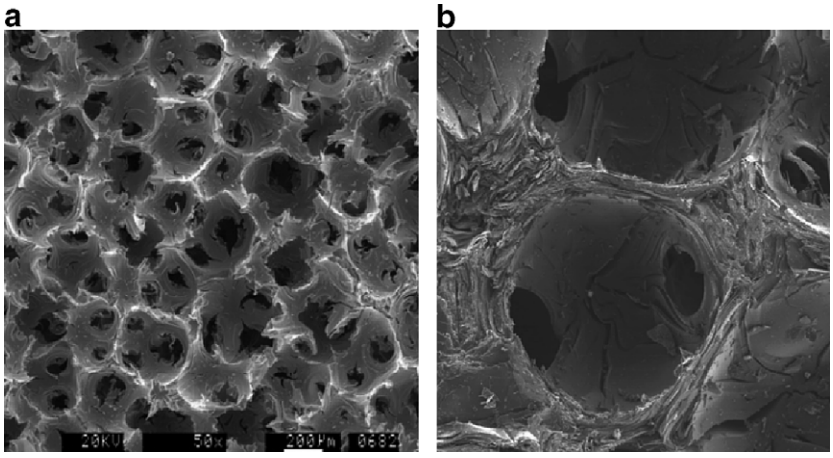

Fig. 1. Klett et al. (2000): (a) Electromicrograph of the graphitic foam surface; (b) Electron micrograph of the graphitic foam surface of a single pore.

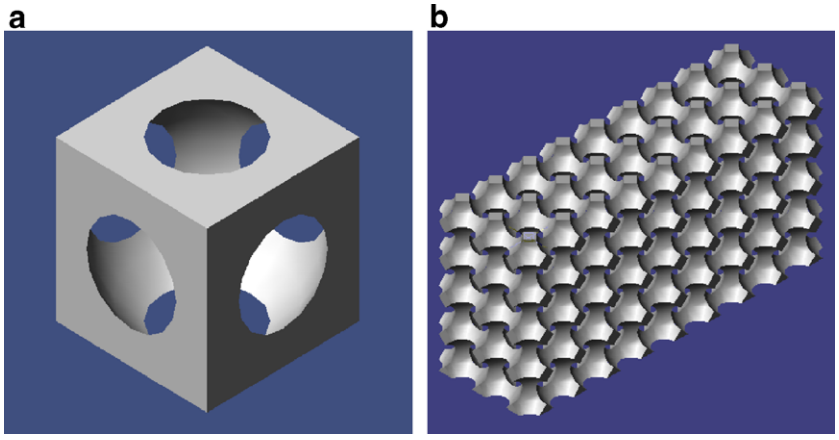

Fig. 2. CAD images showing the unit-cube model (Yu et al., 2006b): (a) A single unit-cube with spherical void; (b) A pore block containing interconnected pores.

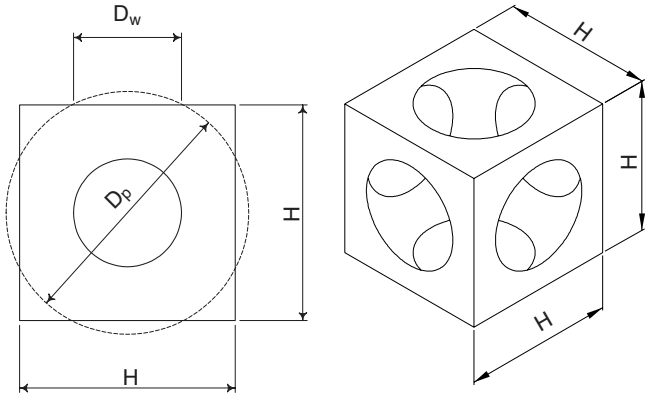

Fig. 3. Detailed dimensions of the unit cube geometry at a cross-section cut at the center plane of the unit-cube cell.

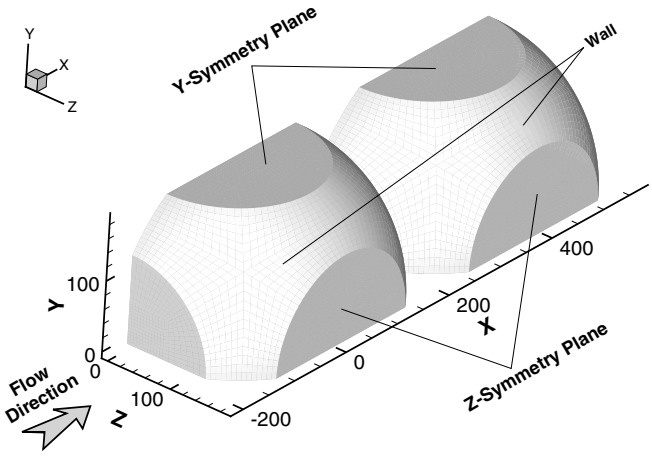

Fig. 4. Computational domain for an idealized SVP foam with $\epsilon = 0.80$.

Using the unit-cube model and by varying the porosity, computational domains for simulating different configurations of spherical-void-phase materials can be generated. The double-periodic cell geometry formulation of Karimian and Straatman (2007) and El Soukkary and Straatman (2003) is used to generate the computational domain. This formulation requires a computational domain comprised of two consecutive periodic cells. Hence, the void phase of two consecutive, interconnected cells is the geometry of interest. Due to the presence of a fully developed steady, laminar flow field with a unidirectional main stream in the X-direction, the computational domain can be reduced to a quarter of the geometric domain without compromising accuracy of the results. Fig. 4 shows an outline of the computational domain for an idealized SVP foam cell with porosity of $\epsilon = 0.80$. The pore windows normal to X-direction are the periodic boundaries.

3. Governing equations and numerical method setup

3.1. Governing equations

Consider an arbitrary fixed control volume $\Omega \subset \mathbb{R}^3$, of volume V and a piecewise smooth boundary $\partial\Omega$, with unit normal surface vector $\hat{n}$ pointing outwards, occupied by an incompressible, Newtonian fluid. The integral form of the conservation equations for mass, momentum and energy is given by

$$\int_{\partial\Omega} \rho \vec{V} \cdot \hat{n}\, \mathrm{d}S = 0, \tag{4}$$

$$\int_{\Omega} \rho \partial_t \vec{V}\, \mathrm{d}V + \int_{\partial\Omega} \hat{n} \cdot (\rho \vec{V}\vec{V})\, \mathrm{d}S - \int_{\partial\Omega} \hat{n} \cdot (\mu \nabla \vec{V})\, \mathrm{d}S = -\int_{\partial\Omega} P\hat{n}\, \mathrm{d}S, \tag{5}$$

$$\int_{\Omega} \rho \partial_t T\, \mathrm{d}V + \int_{\partial\Omega} \hat{n} \cdot (\rho \vec{V} T)\, \mathrm{d}S - \int_{\partial\Omega} \hat{n} \cdot \left(\frac{k}{C_p} \nabla T\right) \mathrm{d}S = 0, \tag{6}$$

where ρ is the density, μ is the viscosity, k is the heat diffusion coefficient (conductivity), C_p is the specific heat, p is the relative pressure, $\vec{V}$ is the velocity vector, T is the absolute temperature, $\mathrm{d}S$ is the surface differential and $\mathrm{d}V$ is the volume differential.

3.2. Discretization method

The parallel code (ParTISUN) developed by Karimian and Straatman (2006) is used to discretize and solve Eqs. (4)–(6) using an implicit, coupled, unstructured finite-volume method. A single-program-multiple-data (SPMD) parallelization model was implemented in the code within the PETSc framework (Balay et al., 2004) to exploit the maximum capability of a cluster of distributed-memory machines. An inexact Jacobian Newton-Krylov (iJNK) method was used in conjunction with the non-linear iterations to accelerate the non-linear convergence in each time-step. The convection term is implicitly modeled using a first-order upstream difference scheme (UDS) and explicitly corrected to higher-order using a deferred-correction technique (Kholsa and Rubin, 1974). In this work, a second-order central difference scheme is selected as a higher-order scheme. However, there is no limit in using other higher-order schemes. The details of the discretization method, parallel implementation and iJNK technique may be found in Karimian and Straatman (2006) and are omitted here for brevity.

3.3. Boundary conditions

All boundary conditions are imposed implicitly (Karimian and Straatman, 2006). A no-slip boundary condition is applied at all walls, i.e, $\vec{V} = 0$ and pressure is extrapolated from inside the domain. In the presence of a solid phase with high conductivity, which is the case in GF, the variation of the wall temperature for two consecutive cells is essentially negligible. Two different length-scales can, therefore, be assumed for the macroscopic solid temperature gradient and the pore-level convective heat transfer. In this case, the length-scale associated with the solid temperature gradient is much larger than that associated

with heat convection mechanism. Of course, when integrating the final convection model into a macroscopic calculation, the pore-level Nusselt number should be considered as a local Nusselt number. Also, in the cross-stream direction, correction models similar to that implemented by using the fin-efficiency analogy can be used to increase the accuracy of macroscopic calculations, see, for example, (Straatman et al., 2007). Therefore, it is reasonable to assume herein a constant wall-temperature condition at the fluid–solid interface of the computational domain.

Symmetry boundary conditions are imposed at the symmetry planes (see Section 2):

$$\begin{cases} \frac{\partial u}{\partial n}=0,\ v=0,\ \frac{\partial w}{\partial n}=0,\ \frac{\partial T}{\partial n}=0, & \text{at } Y\text{-symmetry plane} \\ \frac{\partial u}{\partial n}=0,\ \frac{\partial v}{\partial n}=0,\ w=0, \frac{\partial T}{\partial n}=0, & \text{at } Z\text{-symmetry plane,} \end{cases} \tag{7}$$

where $\vec{V}=\{u,v,w\}$. Pressure is extrapolated from the inside of the domain at all symmetry planes.

A fully developed flow and temperature field is assumed. Therefore, periodic boundary conditions are imposed at the inlet and outlet of the domain. According to the problem of interest, i.e. measurement of pressure drop as a function of mass flow rate, it is desired to specify mass flow rate as a primary inlet condition. The mass flow specified periodic boundary condition proposed by El Soukkary and Straatman (2003) that is based on a double-periodic cell geometry configuration is implemented herein. The mass flow rate is specified at the periodic boundaries. The bulk velocity at the periodic boundaries $U_{\mathrm{b,in}}$ is determined by

$$U_{\mathrm{b,in}}=\frac{A_{\mathrm{b}}}{A_{\mathrm{w}}}V_{\mathrm{ext}}=\frac{4\eta^2}{(1-\eta^2)\pi}V_{\mathrm{ext}}, \tag{8}$$

where $V_{\mathrm{ext}}=\epsilon\times V_{\mathrm{int}}$ is the extrinsic velocity and V_{int} is determined from Eq. (9) by setting the pore-level Reynolds number. Here, A_{b} is the blockage area, A_{w} is the pore-window area and η is the cell ratio (see Eq. 2). The fully developed temperature field does not periodically repeat in each cell. However, an isothermal wall boundary condition, in addition to a fully developed flow, imply periodic behavior in the thermal process. This periodic behavior is the basis of a thermal periodic boundary condition proposed by Karimian and Straatman (2007) that is implemented in this work. Implementation details of the periodic boundary conditions can be found in Karimian and Straatman (2007).

4. The computations

Due to the number and size of the simulations required to develop hydraulic and thermal models, a correct strategy in defining the simulations can save a huge amount of time and effort. Three parameters are varied for each simulation to cover a wide range of idealized thermo-fluid flow regimes and geometries. These three parameters are: Prandtl number, Pr, which characterizes the fluid type, pore-level Reynolds number, Re_{D}, which characterizes the flow regime, and porosity, ϵ, which characterizes the internal geometry (see Section 2). Moreover, grid density and the convergence criteria are influential in the accuracy of results and in the computational cost. In the following, a strategy for the simulation is described in terms of flow regime and fluid type, convergence criteria, grid density and pore-structure range.

It is worth mentioning here that all simulations, including the primary simulations discussed in this section and the main simulations for developing the models, were performed using 16 processors of a distributed-memory cluster of 48 Compaq Alpha processors with a processor speed of 533 MHz and a memory of 1 GB per processor. This cluster was provided by Shared Hierarchical Academic Research Computing Network (SHARCNET: www.sharcnet.ca).

4.1. Flow regimes

There are various definitions of the pore-level Reynolds number available in the literature that are used to describe the flow regimes in porous media. This is mainly because of the variety of the length-scales that can be used in the definition of Reynolds number. These include: particle diameter, equivalent particle diameter, square root of permeability, pore diameter, fiber thickness etc. In fact, because of the variety of microscopic structures for different porous media, there is no way to escape this variation in length-scales. However, four distinct flow regimes are commonly defined in literature in terms of pore-level Reynolds number: Darcy or creeping flow, inertial flow, unsteady laminar flow and chaotic flow regimes. The flow regimes studied in this work are limited to those below unsteady laminar flow. Although there is still a vague definition of pore-level Reynolds number, specifically for this type of geometry, the initial simulations showed that by defining Reynolds number as

$$Re_{\mathrm{D}}=\frac{\rho V_{\mathrm{int}} D_{\mathrm{p}}}{\mu}, \tag{9}$$

where V_{int} is the intrinsic velocity or average pore velocity, a consistent upper limit of $Re_{\mathrm{D}}\approx 1$ for the Darcy flow regime can be observed in a wide range of pore structures. Therefore, pore diameter is selected as a primitive length-scale hereafter and subscript D for a dimensionless quantity indicates that the pore diameter D_{p} is the length-scale in that quantity. As stated before, the limits of Reynolds number at which the flow regimes change vary based on the length-scale and velocity scale used in the formulation of Reynolds number. Hence, it is difficult to select a maximum limit of Reynolds number for the steady laminar flow regime from literature, due to differences in pore structure and length-scale. However, in an experiment performed by Dybbs and Edwards (1984) on flow through packed beds of spheres and packed beds of cylindrical rods, the same range of Reynolds number is observed for Darcy flow, i.e. $Re_d=1$ when Reynolds number is defined as $Re_d=$

$\rho\bar{u}_p\bar{d}/\mu$, where $\bar{u}_p$ is the average pore velocity and $\bar{d}$ is an average characteristic length-scale for the pores. Based on their experiment, the Reynolds number at which unsteady laminar flow starts to form is $Re_d = 150$. This limit is reported by others for other type of porous media, see for example Pedras and de Lemos (2001). In recent experiments, the maximum practical rate of flow through SVP foam achieved was $Re_d \approx 50$ (Straatman et al., 2006). Based on all these facts, an upper limit of $Re_D = 120$, which is safely below any reported unsteady regime and much higher than reported experimental results for SVP foam (Straatman et al., 2006), is an appropriate stopping point for the steady, laminar flow regime. Thus, as an initial target, a range of pore-level Reynolds numbers of $0.1 \leqslant Re_D \leqslant 120$ is selected for the simulations.

4.2. Convergence study

To achieve the same accuracy for mass and momentum equations with the same maximum allowable non-linear residual, each equation in the linear system is normalized by its diagonal coefficient. Moreover, using this normalization technique, once non-linear and steady-state convergence criteria are selected, they can be consistently used for simulations with different geometry parameters to result in essentially the same accuracy. Primary studies on the solution for thermo-fluid flow in the above-mentioned geometry with a range of non-linear and steady-state convergence criteria showed that a maximum non-linear residual of $\xi = 10^{-4}$, with a maximum non-linear iteration of $n_{max} = 10$ per time-step, and a maximum steady-state residual of $\xi_{st} = 10^{-5}$ are deemed satisfactory and no significant change in the results appear by using more restrictive convergence criteria. For more information on the definition of the convergence parameters, please refer to Karimian and Straatman (2006).

4.3. Grid convergence study

A unit-cube model of idealized SVP foam with a porosity of $\epsilon = 0.80$ (the average of the allowable porosity range) was used to conduct a grid convergence study. Four grids with different wall-grid size and number of control volumes were generated inside the double-periodic cell geometry described in Section 2. Table 1 summarizes the grid configurations, where Δ_w is the grid size near the walls. In all cases the maximum-to-minimum edge size $\frac{\Delta_{max}}{\Delta_w}$ does not exceed 3. Fig. 5 shows an outline of Grid 3. Flows with Reynolds numbers of $Re_D = 40$ and $Re_D = 100$ were simulated. Water at a bulk temperature of $T_{b,in} = 300$ K enters the flow field, while a constant wall temperature of $T_w = 350$ K is imposed. According to Table 2, which summarizes the results of the grid convergence study, the results of the computation for Grid 3 are independent of the mesh size. In this table, $\Lambda = (D_p \times \Delta P)/(\mu U_{b,in})$ is the dimensionless pressure drop, Nu_D is the pore-level Nusselt number that is computed for one unit-cube cell (Karimian and Straatman, 2007), $\Delta\Lambda$ is the variation of the dimensionless pressure drop with respect to that for the coarser grid and ΔNu_D is the variation of the pore-level Nusselt number with respect to that for the coarser grid. It is worth mentioning here that the difference between the pressure drop of the first cell and the second cell did not exceed 4% and the difference between the Nusselt number of two consecutive cells was less than 1%.

Table 1
Summary of the grids configuration, grid convergence study

Grid	Grid 1	Grid 2	Grid 3	Grid 4
$\frac{\Delta_w}{D_p}$	$\frac{9}{450}$	$\frac{6}{450}$	$\frac{4}{450}$	$\frac{3}{450}$
No. of CV's	11,000	26,816	84,960	187,207

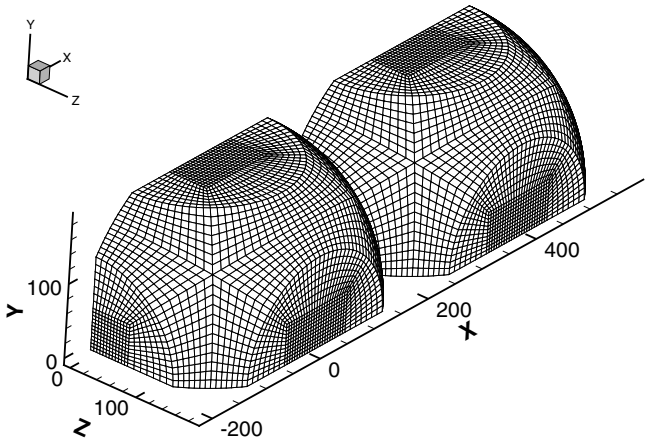

Fig. 5. An outline of Grid 3 with 84,960 control volumes and near-wall-grid size of $\Delta_w = 4$ μm.

Table 2
Nusselt number and pressure drop for different grids, grid convergence study

	Re_D							
	40				100			
	Grid 1	Grid 2	Grid 3	Grid 4	Grid 1	Grid 2	Grid 3	Grid 4
Λ	39.6	40.3	41.0	41.5	47.1	48.0	48.3	48.7
$\Delta\Lambda$		1.7%	1.7%	1.2%		1.9%	<1.%	<1.%
Nu_D	5.024	5.067	5.073	5.073	5.385	5.346	5.301	5.281
ΔNu_D		<1.%	<1.%	0.0%		<1.%	<1.%	<1.%

Fig. 6 shows contours of independent flow and temperature variables at a cross-section between two symmetry planes for a flow with $Re_D = 100$ on Grid 3. The size and the shape of the contour lines in two consecutive cells are essentially identical, which illustrates the achievement of a fully developed, periodic flow field. There is no significant disturbance in the contour lines crossing the outlet and inlet of the computational domain. This can be seen more clearly in Fig. 6b and d. The resemblance of the contour lines crossing the domain inlet and outlet boundaries with those crossing the mid-section proves that the outlet and

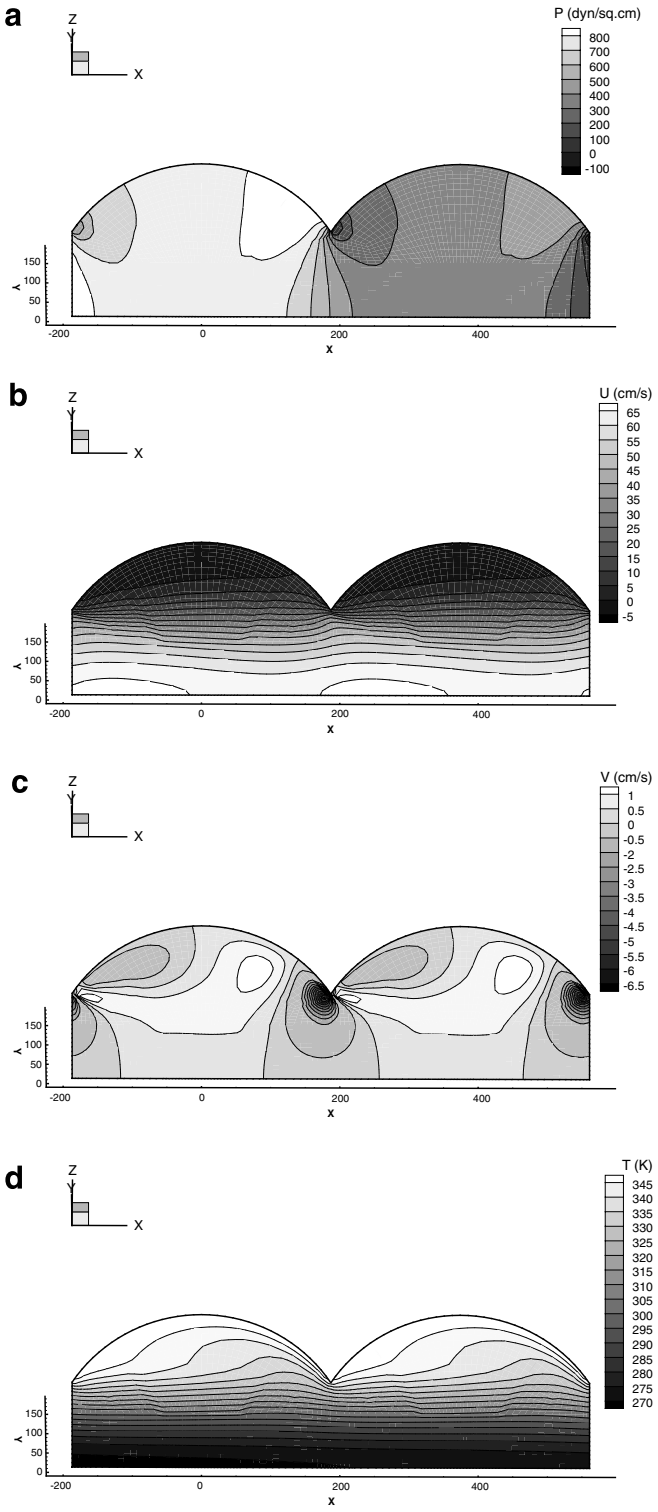

Fig. 6. Contours for (a) pressure, (b) U-velocity, (c) V-velocity and (d) temperature at a cross-section between two symmetry planes (45° from zx-symmetry plane), $Re_D = 100$, Grid 3.

inlet periodic boundaries are essentially transparent to the flow and temperature field.

Based on the observations in grid convergence study, simulations over a grid with wall-grid size of $\frac{\Delta_w}{D_p} = \frac{4}{450}$ and a smooth grid-size variation across the computational domain with a maximum-to-minimum edge size ratio of $\frac{\Delta_{max}}{\Delta_w} \leqslant 3$ is independent of the mesh size and hence this grid configuration is selected for all subsequent computations.

4.4. Porosity range

The range of pore structures used in the simulations must represent the range of pore structures available in reality. According to the unit-cube geometry model (Yu et al., 2006b), a rigid porous media with an interconnected pore structure can be obtained over the range $0.53 \leqslant \epsilon \leqslant 0.96$. However, a more practical limit of porosity based on available SVP foams is about $0.75 \leqslant \epsilon \leqslant 0.90$. For a given fluid and Reynolds number, 4 simulations with different porosities of $\epsilon = 0.75$, 0.80, 0.85 and 0.90 are performed.

Combinations of the above-mentioned flow rates, fluid types and porosities formed 168 separate simulations, which resulted in a wide range of pressure drop and pore-level Nusselt number Nu_D data. For a combination of each geometry configuration and fluid, 14 simulations with pore-level Reynolds numbers of $Re_D = 0.1$, 0.4, 0.7, 1.0, 4.0, 7.0, 10, 25, 40, 55, 70, 85,100 and 120 are performed to cover the flow regimes considered. To correlate the pore-level Nusselt number Nu_D with the Prandtl number Pr, simulations are also carried out for three different Prandtl numbers of $Pr = 5.85$ (water), $Pr = 3.45$ (Freon-12) and $Pr = 0.706$ (air). Results from this data set are used in the following sections to develop hydraulic and thermal models.

5. Semi-heuristic models

5.1. Hydraulic model

The hydraulic behavior of creeping flow through a generic porous media shows a linear relationship between pressure drop and velocity. By defining the permeability, κ, for a homogeneous porous media, Darcy (1856) proposed the following linear relation, known as Darcy's law, for unidirectional flow through a porous media with a thickness of L:

$$-\frac{\Delta P}{L} = \frac{\mu}{\kappa} V_{ext}, \tag{10}$$

As the flow rate increases, a deviation from Darcy's law appear in the behavior of the pressure drop in terms of velocity. This deviation indicates a change from a viscous dominant (creeping) flow to an inertia dominant (strong inertia) flow regime. To characterize the non-linear behavior in the strong inertia regime, Forchheimer (1901) proposed a second-order formula:

$$-\frac{\Delta P}{L} = \frac{\mu}{\kappa} V_{ext} + \frac{\beta}{\sqrt{\kappa}} \rho V_{ext}^2, \tag{11}$$

where β is non-Darcy flow coefficient.

To relate the permeability κ and the non-Darcy flow coefficient β to the pore-structure geometry, many analytical and semi-heuristic models have been proposed (Dullien, 1979; Kaviany, 1999). The Carman–Kozeny model (Dullien, 1979), however, appears to be the most popular and successful model to define the permeability as a function of geometry for porous media with a moderate porosity. The Carman–Kozeny model was initially developed for creeping flow in a packed bed of spherical particles. In their model, the pore geometry is assumed to be a conduit with an extremely complicated shape but an averagely constant area. However, regardless of this condition, both the model and its basic concept have been used for modeling Darcy flow through other pore structures. Using the concept of hydraulic diameter, a Hagen–Poiseuille type equation was solved for the permeability of a packed bed (Kaviany, 1999):

$$\frac{\kappa}{d^2} = \frac{\epsilon^3}{36k_K(1-\epsilon)^2}. \tag{12}$$

Here, d is the mean or equivalent particle diameter and k_K is the Kozeny constant. The Kozeny constant represents the shape factor and the deviation of flow direction from that in a duct and is approximated as 5 for packed beds but varies strongly as a function of porosity for other internal structures, see for example Sahraoui and Kaviany (1992) and Happel and Brenner (1986) among others.

To model the non-Darcy coefficient β, Ergun (1952) extended Carman–Kozeny theory to the strong inertia flow regime and, by comparing viscous forces against inertia forces and defining a modified friction factor as

$$f' = \frac{\Delta P}{\rho V_{ext}^2} \cdot \frac{d}{L} \cdot \frac{\epsilon^3}{1-\epsilon} \tag{13}$$

and a modified Reynolds number as

$$Re' = \frac{\rho d V_{ext}}{\mu} \cdot \frac{1}{1-\epsilon}, \tag{14}$$

he found that an equation of the form:

$$f' = \frac{A}{Re'} + B, \tag{15}$$

fits the data over a wide range of Reynolds numbers. Here, A is proportional to Kozeny constant k_K and B is the extended Ergun coefficient. The extended Ergun coefficient is reported to be $B = 1.8$–4.0 depending on the internal structure and the porosity (Dybbs and Edwards, 1984).

Since the internal structure of a spherical-void-phase porous media is significantly different with that of a packed bed of spherical particles, the parameters governing the permeability model of graphitic foam are presumably different with those governing the Carman–Kozeny model. Therefore, Carman–Kozeny theory must be re-visited to develop a suitable extended model for SVP foam.

In spite of a good engineering approximation provided by a quadratic relation such as Darcy–Forchheimer equation (Eq. (11)) for steady laminar flow regime, it is experimentally shown (Muskat, 1946) among others that in the presence of a weak inertia flow ($Re \to 0$), the pressure behavior is cubic with respect to velocity. Muskat divided the steady laminar flow regime into three zones: Darcy zone, where Darcy's law prevails, transition zone, where weak inertia flow appears with quadratic behavior of pressure gradient in terms of Reynolds number (cubic behavior in terms of velocity) and linear deviation zone, where strong inertia flow regime appears with linear behavior of pressure gradient in terms of Reynolds number (quadratic behavior in terms of velocity). Moreover, Mei and Auriault (1991) solved the Navier–Stokes equations for weak inertia flows using the concept of the theory of homogenization and showed that the pressure drop in this zone varies quadratically with velocity. Firdaouss et al. (1997) re-assessed some legendary experiments including that of Darcy and Forchheimer and proved that those experiments qualitatively follow the cubic model proposed by Mei et al. for weak inertia flows. Moreover, Firdaouss et al. (1997) suggested that "the Darcy zone and the transition zone emphasized by Muskat merge into one unique zone, which corresponds to the asymptotic behavior $Re \to 0$".

In this section, Carman–Kozeny theory is followed to recognize important geometry parameters characterizing flow behavior in SVP foam for steady laminar flow regime. Moreover, the presence of a weak inertia flow regime with a cubic pressure behavior in this type of porous media is explored, but not included in the engineering model.

5.1.1. Extended-permeability model

It is convenient to study the dimensionless form of the equations. Taking the Darcy–Forchheimer relation as a starting point and defining the normalized pressure drop as

$$\Pi_D = -\left(\frac{\Delta P}{H}\right) \times \left(\frac{D_p^2}{\mu V_{ext}}\right), \tag{16}$$

Eq. (11) can be re-written in the dimensionless form of

$$\Pi_D = \frac{1}{K_D} + \epsilon \frac{\beta}{\sqrt{K_D}} Re_D, \tag{17}$$

where Re_D is the pore-level Reynolds number (defined by Eq. 9) and K_D is the normalized permeability based on pore diameter and is defined as

$$K_D = \frac{\kappa}{D_p^2}. \tag{18}$$

Eq. (17) shows that the dimensionless form of a second-order polynomial in terms of velocity is a linear equation in terms of Reynolds number. Fig. 7 depicts the variation of normalized pressure drop Π_D with pore-level Reynolds number Re_D for the data from all the simulations. In this figure, W indicates water, F indicates Freon-12 and A indicates air. The data covers a wide range of Reynolds numbers and porosities. As can be seen, the overall shape of the pressure diagram is similar for various porosities, which indicates that a similar form of relation can model this

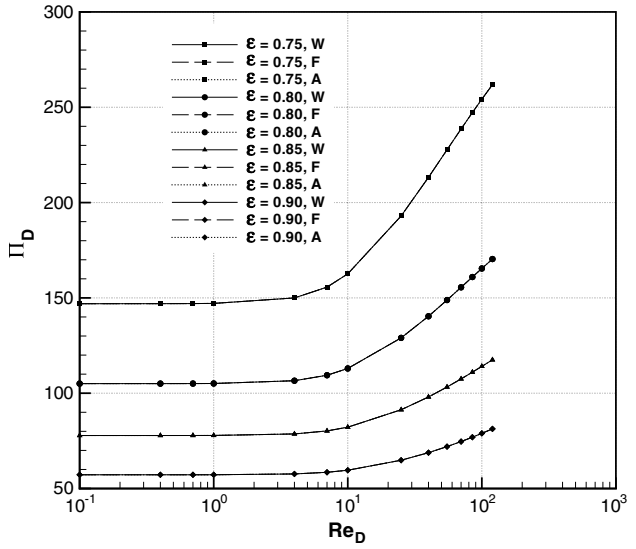

Fig. 7. Normalized pressure drop vs. pore-level Reynolds number.

behavior for the range $0.75 \leqslant \epsilon \leqslant 0.90$. Moreover, Fig. 7 shows that the first term of Eq. (17) can model the pressure variation for $Re_D \leqslant 1$. It is clear from Fig. 7 that the normalized pressure drop Π_D is independent of the fluid type, as expected. Therefore, according to Eq. (17), the normalized permeability K_D and the non-Darcy flow coefficient β are solely functions of porosity ϵ. Thus, it is of interest herein to find these two coefficients as functions of porosity.

Carman–Kozeny theory uses the analogy of fully developed flow in a duct. Assume that for creeping flow, a Hagen–Poiseuille type equation can approximate the pressure drop in terms of intrinsic velocity, that is to say

$$-\frac{\Delta P}{L_e} = \frac{16 k_0 \mu}{D_h^2} V_p, \tag{19}$$

where L_e is the average length of a path-line across a cell (from inlet to outlet), k_0 is a shape factor, V_p is the average pore velocity, $V_p = (L_e/H) \times V_{int}$, and D_h is the hydraulic diameter of a cell, $D_h = 4 \times V_f/A_{fs}$. Here, $V_f = \epsilon \times H^3$ is the void (or fluid) volume of a cell and the wetted surface area is calculated using the following equation (Yu et al., 2006b):

$$A_{fs} = \pi(3\eta - 2)D_p^2. \tag{20}$$

Hence,

$$D_h = \frac{4\epsilon\eta^3}{\pi(3\eta - 2)} D_p. \tag{21}$$

Moreover, define the tortuosity ratio $\tau = L_e/H$. Therefore, $V_p = (\tau/\epsilon) \times V_{ext}$ and thus

$$-\frac{\Delta P}{H} = \frac{(k_0 \tau^2 \pi^2)(3\eta - 2)^2 \mu}{\epsilon^3 \eta^6 D_p^2} V_{ext} \tag{22}$$

or

$$\Pi_D = \frac{(k_K \pi^2)(3\eta - 2)^2}{\epsilon^3 \eta^6}, \tag{23}$$

where $k_K = k_0 \tau^2$ is the Kozeny constant. As mentioned earlier, the Kozeny constant is not necessarily constant with porosity, since the mean path length L_e can vary considerably with porosity even if the shape of the pore structure is essentially similar for different porosities. It is now reasonable to define a modified pressure drop as

$$\Psi_D = \frac{\epsilon^3 \eta^6}{(3\eta - 2)^2} \Pi_D. \tag{24}$$

Therefore,

$$\Psi_D = k_K \pi^2. \tag{25}$$

An extended-permeability model can then be proposed by adding an Ergun-like extension:

$$\Psi_D = k_K \pi^2 + E_r Re_D, \tag{26}$$

where E_r is an Ergun-like coefficient.

To verify the proposed model, a linear curve of

$$\Psi_D = A\pi^2 + BRe_D \tag{27}$$

is fitted on the data presented in Fig. 7 and the coefficients A and B are evaluated as functions of porosity. Fig. 8 shows the variation of the coefficients A and B with porosity ϵ. It can be shown that for a range of $0.75 \leqslant \epsilon \leqslant 0.90$,

$$B' = \sqrt{1 - \eta^2} \times B = \text{Const.} \tag{28}$$

and $B' \approx 0.25$. Therefore, by defining

$$A' = (1 - \eta^2) \times A, \tag{29}$$

Eq. (27) can be re-written in the form of

$$\Psi_D \times (1 - \eta^2) = A'\pi^2 + B' \times \sqrt{1 - \eta^2} Re_D. \tag{30}$$

Eqs. (30) and (3) indicate that the pore-window diameter D_w is a better choice as a length-scale characterizing the pore-level flow dynamics. Hence, the pore-window diame-

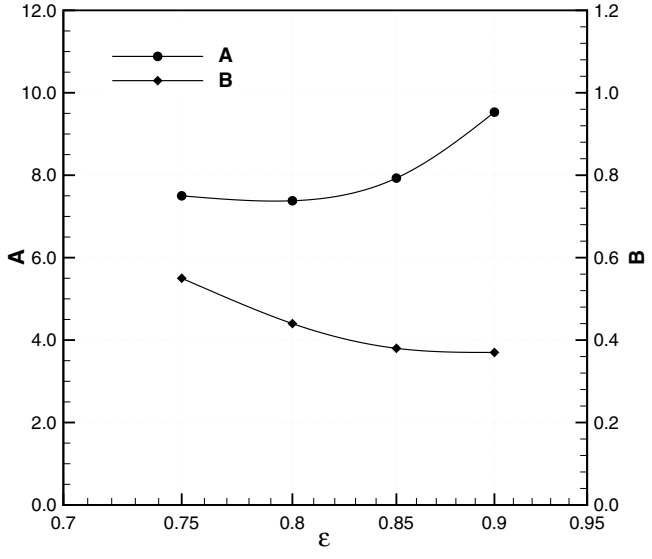

Fig. 8. Curve fitting coefficients A and B vs. porosity.

ter D_w is selected as the pore-level length-scale and therefore, Eq. (30) becomes

$$\Psi_W = A'\pi^2 + B'Re_W, \tag{31}$$

where the pore-window Reynolds number, Re_W, can be computed using Eq. (9) and by replacing D_p with D_w and

$$\Psi_W = \frac{\epsilon^3\eta^6}{(3\eta-2)^2}\Pi_W. \tag{32}$$

Here, the dimensionless pressure drop based on pore-window diameter, Π_W, is calculated using Eq. (16) and by replacing D_p with D_w. Comparing Eq. (31) with Eq. (26), one can define a modified Kozeny constant as $k'_K = A'$ and a modified Ergun-like coefficient as $E'_r = B'$ and thus:

$$\Psi_W = k'_K\pi^2 + E'_r Re_W. \tag{33}$$

Fig. 9a shows the variation of the modified Kozeny constant k'_K with porosity. The increasing trend of k'_K with porosity is consistent with that found for other structures Kaviany, 1999, p. 37. Fig. 9b shows the variation of the non-Darcy modified pressure drop, $\Psi_W - k'_K\pi^2$, with the pore-window Reynolds number Re_W. This figure illustrates that the modified pressure drop Ψ_W is the main characteristic parameter of the flow and the proposed model can predict the data to a good approximation. The model predicts the data from the simulation with less than 10% deviation.

The dimensionless form of the Darcy–Forchheimer relation based on the pore-window diameter can then be written as

$$\Pi_W = \frac{1}{K_W} + \epsilon\frac{\beta}{\sqrt{K_W}}Re_W. \tag{34}$$

Here, the normalized permeability based on pore-window diameter, $K_W = \kappa/D_W^2$, is calculated using the relation:

$$K_W = \frac{\epsilon^3\eta^6}{k'_K\pi^2(3\eta-2)^2} \tag{35}$$

and thus,

$$\frac{\kappa}{D_W^2} = \frac{\epsilon^3\eta^6}{k'_K\pi^2(3\eta-2)^2}. \tag{36}$$

The non-Darcy flow coefficient β is

$$\beta = \frac{(3\eta-2)}{\pi\eta^3\sqrt{\epsilon k'_K}}E'_r. \tag{37}$$

A comparison between the Carman–Kozeny model for packed beds of spherical particles (Eq. (12)) and the modified Carman–Kozeny model for SVP foam (Eq. (36)) shows that not only the length-scale in two geometries are different, the mean particle diameter d in the former and the pore-window diameter D_W in the latter, but also the form of the equation for the model varies dramatically. This is mainly because in SVP foam the internal surface area is cut with six interconnected pore windows and thus is geometrically different than the fluid–solid interface area of a particle in a packed bed of spherical particles. Therefore, whereas defining an equivalent particle diameter for SVP foam, as proposed by Yu et al. (2006b), may provide a good correlation for a range of porosity ϵ, the modified Carman–Kozeny model proposed herein by Eq. (36) is more reasonable due to its mathematical basis.

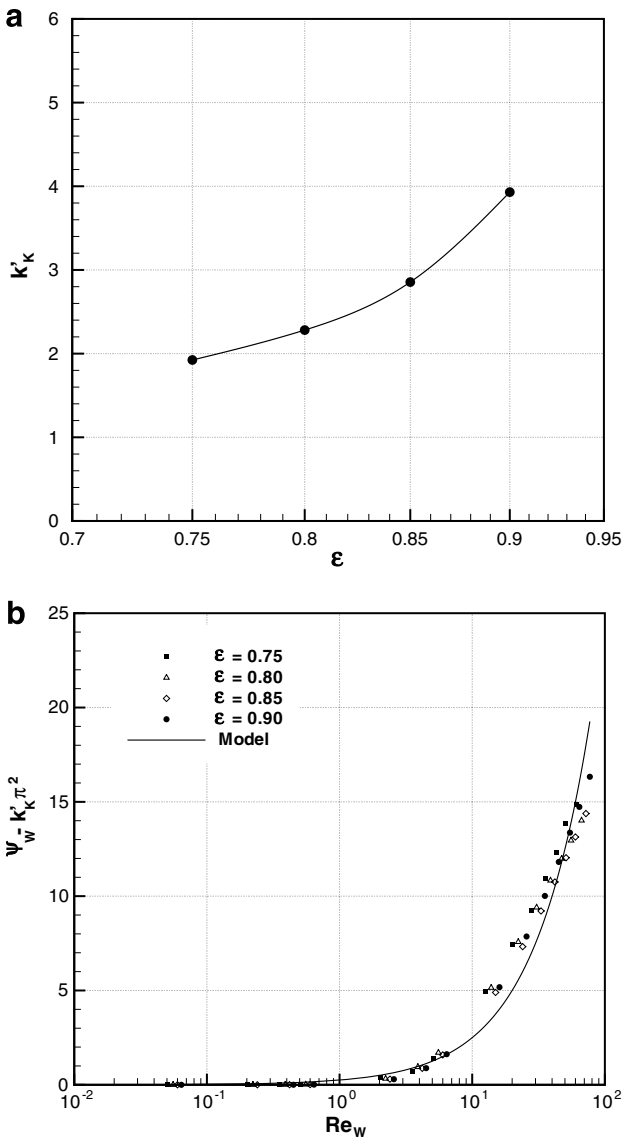

Fig. 9. (a) Modified Kozeny constant K'_K vs. porosity; (b) the non-Darcy modified pressure drop vs. pore-window Reynolds number.

It is noteworthy that the computed quantities of k'_K and E'_r herein are for a foam with an idealized spherical-void structure, and cannot therefore be applied to a real foam without further calibration. However, the fact that the modified pressure drop Ψ_W characterizes the hydraulic behavior of the pore-level flow in SVP foam is clearly illustrated and this can be extended for use with an empirical model.

5.1.2. Weak inertia flow

To explore the presence of a weak inertia zone with a quadratic behavior of pressure drop in terms of pore-level

Reynolds number, the following normalization procedure suggested by Firdaouss et al. (1997) is performed on the results for $0.1 \leqslant Re_D \leqslant 10$ (a potential weak inertia zone):

$$x = \frac{Re_W}{Re_{W,max}}, \tag{38}$$

where x is the flow index and $Re_{W,max}$ is the pore-window Reynolds number corresponding to $Re_D = 10$. Furthermore, a non-Darcy pressure index is defined by this procedure as

$$y = \frac{\Psi_W - k'_K \pi^2}{\Psi_{W,max} - k'_K \pi^2}. \tag{39}$$

Here, $\Psi_{W,max}$ is the modified pressure drop at $Re_{W,max}$. Using this definition we have

$$y = a_1 x + a_2 x^2 + a_3 x^3 + \cdots, \tag{40}$$

where $\sum a_i = 1$. The size of the coefficients a_i can be used as a measure for determining the hydraulic behavior of the flow. If the data are on the line $y = x$, the pressure behavior will be linear in terms of pore-level Reynolds number and if a_2 is not negligible, the behavior will be quadratic. Note that, although Eq. (40) reveals the nature of the hydraulic behavior, it cannot be used as a model, since the indices x and y are normalized by $Re_{W,max}$ and $\Psi_{W,max} - k'_K \pi^2$, respectively.

Fig. 10 shows the pressure index y vs. the flow index x for the data from the simulations. In this figure, all data fit on one curve, which again shows that the modified pressure drop Ψ_W characterizes the hydraulic behavior of the pore-level flow for a range of $0.75 \leqslant \epsilon \leqslant 0.90$. Moreover, the shape of the curve shows that the hydraulic behavior of the weak inertia flow is not linear. A curve fit process reveals that the coefficient a_2 is the dominant coefficient, regardless of the degree of polynomial. This shows qualitatively that a weak inertia flow regime with a quadratic hydraulic behavior in terms of microscopic Reynolds number as suggested by Mei and Auriault (1991) and Firdaouss et al. (1997), among others, exists amid flow through a spherical-void-phase porous media.

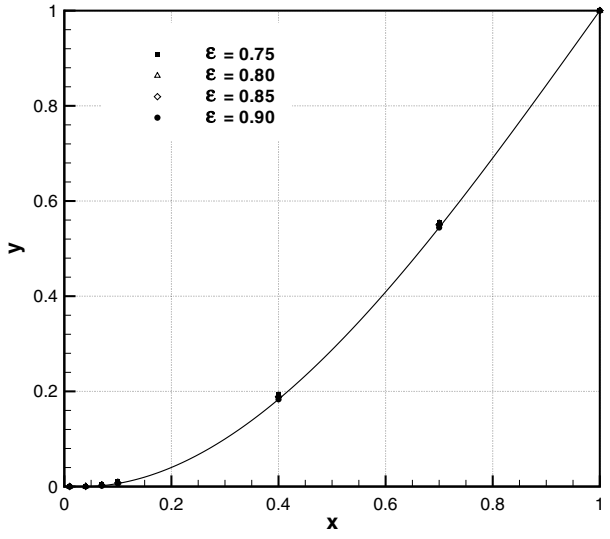

Fig. 10. Pressure index y vs. flow index x.

5.2. Convective heat transfer model

The accuracy of the calculation of the pore-level convective heat transfer depends highly on the presence of a non-equilibrium thermal condition. This condition prevails when the solid heat conduction rate is much higher than the rate at which the interstitial heat transfer happens at the fluid–solid interface. A considerable temperature difference between solid and fluid phase and a high flow Peclet number are required to make a non-equilibrium thermal condition. Therefore, the results for low flow Peclet numbers are not accurate. In fact, because of the uncertainty associated with heat transfer measurements in low Peclet number flows, there has been always a question in the asymptotic thermal behavior of the flow in that region (Kaviany, 1999, p. 404). The fact that a thermal non-equilibrium condition is not valid makes the presence of convective heat transfer questionable in this regime. The least one can say is that the contribution of the molecular heat diffusion in this zone is comparable to that of heat convection. Therefore, the model developed herein is based on the results of the simulations for flow with high Peclet numbers ($Pe \gg 1$).

The cell-based convective heat transfer coefficient for periodic thermo-fluid flow in cell, $\bar{h}_c$, as defined in Karimian and Straatman (2007) for constant wall-temperature condition, is calculated for each simulation. Since the pore-window diameter is selected as the microscopic length-scale, the pore-window Nusselt number is calculated as

$$Nu_W = \frac{\bar{h}_c D_w}{k}, \tag{41}$$

where k is the heat diffusion coefficient of the fluid. In Fig. 11, the variation of the pore-window Nusselt number with pore-level Peclet number, Pe_W is shown for the results of the simulations. The pore-level Peclet number is defined as

$$Pe_W = Re_W \times Pr. \tag{42}$$

In this plot, the data items are grouped in four curves of constant porosity, regardless of the Prandtl number Pr, which shows that the pore-window Nusselt number is a function of the pore-level Peclet number:

$$Nu_W = f(Pe_W, \text{pore geometry}). \tag{43}$$

Moreover, each curve asymptotically approaches a constant value. The asymptotic behavior of heat convection can be discussed as follows: In the creeping flow regime (see Fig. 12a), a thick boundary layer forms alongside the walls, and the molecular diffusion is the dominant heat transfer mechanism. As the Peclet number increases (by increasing Reynolds number) the boundary layer thickness

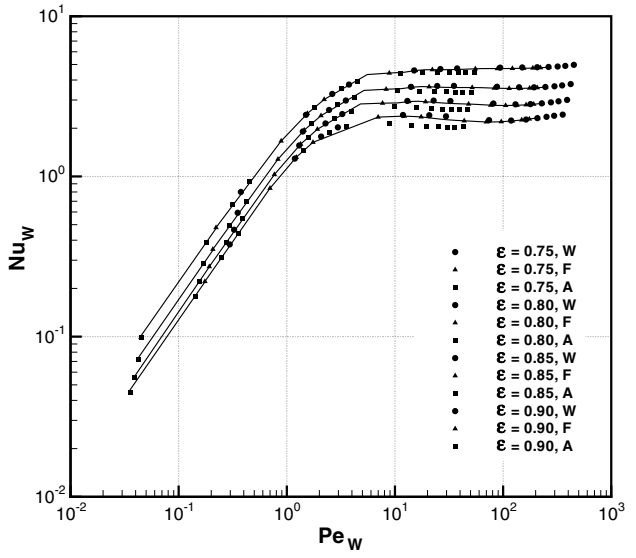

Fig. 11. Pore-window Nusselt number vs. pore-level Peclet number.

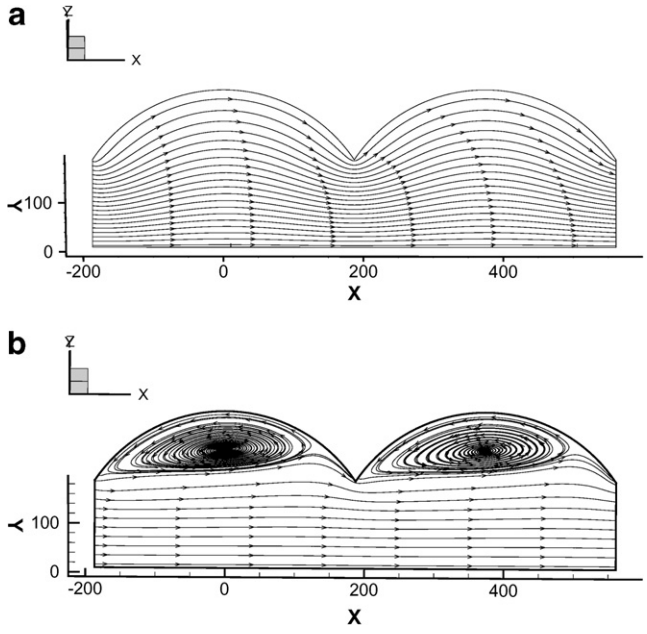

Fig. 12. Streamlines at a cross-section 45° from zx-symmetry plane for the case of (a) $Re_D = 0.1$ and (b) $Re_D = 25$, Grid 3.

decreases resulting in an increase in the temperature gradient normal to the walls and hence an increase in heat conduction. As the flow rate increases, a separation bubble starts to form inside the opening in the flow field, downstream of the inflow pore window. The separation bubble acts as an insulator and, therefore, a decrease in the slope of *Nu* vs. *Pe* plot occurs (see Fig. 11). Since the flow circulation in the separation bubble removes the heat from the mainstream and releases it to the solid wall, or vice versa, the dominant heat transfer mechanism in the bubble is switched to heat convection by means of flow circulation. The size of the separation bubble grows with increasing flow rate until it reaches to its maximum size, occupying the whole opening near the pore window normal to the flow direction (see Fig. 12b.) From this point on the flow structure will not vary significantly with flow rate resulting in an asymptotic behavior in *Nu* vs. *Pe* plot.

As mentioned before, the accuracy of the Nusselt number calculated for low Peclet numbers is questionable. Therefore, the convective heat transfer model proposed herein is limited to the strong inertia thermo-fluid flow regime with $Pe \gg 1.0$ (the asymptotic zone in Fig. 11) and it is assumed that

$$Nu_W = f(\text{pore geometry}) \quad \text{for } Pe \gg 1. \tag{44}$$

Fig. 13 shows the asymptotic value for each porosity. The form of the dependency of the pore-window Nusselt number to the geometry is still unknown. The variation of the porosity leads to the variation of the pore-window diameter and the variation of the internal surface area. The pore-window diameter is the characteristic length-scale at pore-level and the internal surface area is the means for solid-to-fluid heat transfer. Both of these parameters are already included in the definition of the pore-window Nusselt number: the former is the length-scale on which the Nusselt number is based and the latter is used in calculating the cell-based convective heat transfer coefficient $\bar{h}_c$. However, due to the non-linear nature of convective heat transfer, it is expected that the dependency of the pore-window Nusselt number Nu_W to the porosity ϵ can be expressed in the form of (see Eqs. (20) and (3))

$$Nu_W = a(3\eta - 2)^m(1 - \eta^2)^n \quad \text{for } Pe \gg 1. \tag{45}$$

By a curve fitting process to the present computational data, it is shown that

$$Nu_W = \frac{3.10(1 - \eta^2)^{0.5}}{(3\eta - 2)^{0.725}} \quad \text{for } Pe \gg 1. \tag{46}$$

Therefore, from Eq. (3), we can also form

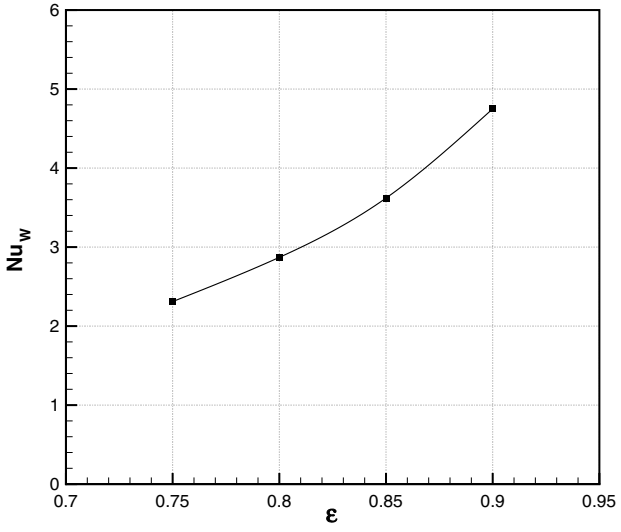

Fig. 13. Pore-window Nusselt as a function of porosity.

$$Nu_D = \frac{3.10}{(3\eta - 2)^{0.725}} \quad \text{for } Pe \gg 1, \tag{47}$$

where Nu_D is the pore-level Nusselt number based on D_p

$$Nu_D = \frac{\bar{h}_c D_p}{k}. \tag{48}$$

Hence the characteristic length-scale in pore-level heat transfer is the pore diameter D_p. Also, for $Pe \gg 1.0$, the dependency of the convective heat transfer coefficient to the flow is insignificant and it is only a function of the geometry and can be expressed in a general form of

$$Nu_D = \frac{A}{(3\eta - 2)^n} \quad \text{for } Pe \gg 1, \tag{49}$$

where parameters A and n can be calibrated using experimental measurements.

6. Conclusion

A set of simulations of the pore-level thermo-fluid flow in a spherical-void-phase porous media have been carried out to better understand the hydraulic and thermal behavior of the flow. A permeability model was developed for the interconnected spherical-void geometry based on Carman–Kozeny theory and an Ergun-like, non-linear extension was added to the model. Using this analogy revealed that three geometric parameters govern the hydraulic behavior of the microscopic flow: pore-window diameter, porosity and the cell ratio (the ratio of the cell size to the pore diameter). Although the cell ratio is solely a function of the porosity, due to the complexity of the function, it is not included in the model and the model is developed as a function of the cell ratio. The difference between the proposed modified Carman–Kozeny model for SVP foam with the original one for packed beds of spherical particles can be expressed mathematically based on the difference between two geometries. The variation of the proposed Kozeny constant with porosity is in agreement with others in literature. Moreover, a weak inertia flow region was recognized with a quadratic pressure behavior in terms of pore-level Reynolds number (or cubic in terms of velocity). The results of the simulations for the weak inertia flow is in agreement with the weak inertia theory of Mei and Auriault (1991) and the results of Firdaouss et al. (1997). A combination of a linear permeability model and a quadratic Ergun-like extension is still recommended as a good engineering approximation for both weak and strong inertia flow. By using the concept of periodicity (Karimian and Straatman, 2007), the pore-level Nusselt number for a cell is calculated. An asymptotic behavior is observed for the convective heat transfer coefficient as a function of Peclet number. This behavior is discussed to be a result of the development of a separation bubble in the flow field. The pore-level Nusselt number is characterized using the pore diameter as a length-scale. A heat transfer model is proposed for strong inertia flow regime relating the pore-level Nusselt number to the pore-structure geometry is also proposed, subject to calibration with experimental data.

Acknowledgements

The authors gratefully acknowledge the financial support from the Natural Science and Engineering Research Council (NSERC) and from SHARCNET.

References

Balay, S., Buschelman, K., Eijkhout, V., Gropp, W.D., Kaushik, D., Knepley, M.G., McInnes, L.C., Smith, B.F., Zhang, H., 2004. PETSc users manual. Tech. Rep. ANL-95/11 - Revision 2.1.5, Argonne National Laboratory.

Boomsma, K., Poulikakos, D., Ventikos, Y., 2003. Simulations of flow through open cell metal foams using an idealized periodic cell structure. International Journal of Heat and Fluid Flow 24, 825–834.

Calmidi, V., Mahajan, R., 1999. The effective thermal conductivity of high porosity fibrous metal foam. ASME Journal of Heat Transfer 121, 466–471.

Calmidi, V., Mahajan, R., 2000. Forced convection in high porosity metal foams. ASME Journal of Heat Transfer 122, 557–565.

Darcy, H., 1856. Les Fontaines Publiques de la ville de Dijon. Dalmont, Paris.

Dullien, F., 1979. Porous Media: Fluid Transport and Pore Structure. Academic Press.

Dybbs, A., Edwards, R., 1984. A new look at porous media fluid mechanics – Darcy to turbulent. In: Bear, J., Coraocioglu, M.Y. (Eds.), Fundamentals of transport phenomena in porous media, NATO ASI Series, Series E: Applied Sciences, 82. Martinus Nujhoff Publishers, pp. 199–254.

El Soukkary, T., Straatman, A.G., 2003. The prediction of spatially periodic flows using a finite-volume model. International Journal for Numerical Methods in Fluids 41, 303–317.

Ergun, S., 1952. Fluid flow through packed volumes. Chemical Engineering Progress 89, 48.

Firdaouss, M., Guermond, J.-L., Le Quéré, P., 1997. Nonlinear corrections to Darcy's law at low Reynolds numbers. Journal of Fluid Mechanics 343, 331–350.

Forchheimer, P., 1901. Wasserbewegung durch boden. Z. Vereines deutscher Ingnieure XXXXV, 49, 1736–1741 and 50, 1781–1788.

Fourar, M., Radilla, G., Lenormand, R., Moyne, C., 2004. On the non-linear behavior of a laminar single-phase flow through two and three-dimensional porous media. Advances in Water Resources 27, 669–677.

Fourie, J., Du Plessis, J., 2002. Pressure drop modelling in cellular metallic foams. Chemical Engineering Science 57, 2781–2789.

Gallego, C., Klett, W., 2003. Carbon foams for thermal managements. Carbon 41, 1461–1466.

Happel, J., Brenner, H., 1986. Low Reynolds number hydrodynamics. Martinus Nijhoff Publishers.

Incropera, F.P., DeWitt, D.P., 2002. Fundamentals of Heat and Mass Transfer, fifth ed. John Wiley & Sons.

Karimian, S.A.M., 2006. Computational modelling of the flow and heat transfer in an idealized porous metal. Ph.D. Dissertation, The University of Western Ontario, London, Ontario, Canada, April.

Karimian, S.A.M., Straatman, A.G., 2006. Discretization and parallel performance of an unstructured finite volume Navier–Stokes solver. International Journal for Numerical Methods in Fluids 52 (6), 591–615.

Karimian, S.A.M., Straatman, A.G., 2007. A thermal periodic boundary condition for heating and cooling processes. International Journal of Heat and Fluid Flow 28, 329–339.

Kaviany, M., 1999. Principles of Heat Transfer in Porous Media, second ed. Springer.

Kholsa, P., Rubin, S., 1974. A diagonally dominant second-order accurate implicit scheme. Computers and Fluids 2, 207–209.

Kim, J., Lee, J., Lee, K.-C., 2001. Nonlinear correction to Darcy's law for a flow through periodic arrays of elliptic cylinders. Physica A 293, 13–20.

Klett, W., Hardy, R., Romine, E., Walls, C., Burchell, T., 2000. High-thermal conductivity, mesophase-pitch-derived carbon foam: effect of precursor on structure and properties. Carbon 38, 953–973.

Mei, C., Auriault, J.-L., 1991. The effect of weak inertia on flow through a porous medium. Journal of Fluid Mechanics 222, 647–663.

Muskat, M., 1946. The flow of homogeneous fluids through porous media. The Mapple Press Company, York, PA.

Pedras, M.H., de Lemos, M.J., 2001. Macroscopic turbulence modeling for incompressible flow through undeformable porous media. International Journal of Heat and Mass Transfer 44, 1081–1093.

Rojas, S., Koplik, J., 1998. Nonlinear flow in porous media. Physical Review E 58 (4), 4776–4782.

Sahraoui, M., Kaviany, M., 1992. Slip and no-slip boundary condition at interface of porous, plain media. International Journal of Heat and Mass Transfer 35, 927–943.

Spena, F.R., Vacca, A., 2001. A potential formulation on non-linear models of flow through anisotropic porous media. Transport in Porous Media 45, 407–423.

Straatman, A., Yu, Q., Gallego, N., Thompson, B., 2006. Characterization of porous carbon foam as a material for compact recuperators. In: Proceedings of TURBO Expo 2006. ASME Turbo Expo.

Straatman, A.G., Gallego, N.C., Yu, Q., Betchen, L., Thompson, B.E., 2007. Forced convection heat transfer and hydraulic losses in porous carbon foam. ASME Journal of Heat Transfer, in press.

Tadrist, L., Miscevic, M., Rahli, O., Topin, F., 2004. About the use of fibrous materials in compact heat exchangers. Experimental Thermal and Fluid Science 28, 193–199.

Yu, Q., Straatman, A.G., Thompson, B.E., 2006a. Carbon-foam finned tubes in air-water heat exchangers. Applied Thermal Engineering 26 (2–3), 131–143.

Yu, Q., Thompson, B.E., Straatman, A.G., 2006b. A unit cube-based model for heat transfer and fluid flow in porous carbon foam. ASME Journal of Heat Transfer 128, 352–360.